Inorganic Chemistry

Article

pubs.acs.org/IC

Electron Counting Rules and Electronic Structure in Tetrameric Transition-Metal (T)-Centered Rare-Earth (R) Cluster Complex Halides (X)

Simon Steinberg,[†,‡] Thomas Bell,[†] and Gerd Meyer*[,†,§]

[†]Department of Chemistry, Inorganic Solid State and Coordination Chemistry, Universität zu Köln, Greinstaße 6, 50939 Köln, Germany

[‡]Department of Materials Science and Engineering and [§]Department of Chemistry, Iowa State University, Ames, Iowa 50011, United States

Supporting Information

ABSTRACT: Electron partition schemes are a beneficial means to systematize bonding networks and to identify structure-bonding relationships in polar intermetallics. One prolific class of polymetal networks with simple counterions is the broad family of transition-metal (T)-centered rare-earth metal (R) cluster halides (X), which can be isolated or condensed to oligomers and chains. While the electronic structures of R cluster monomers and chains encapsulating T atoms have been studied systematically, the band structures of oligomers, in particular, the most frequent Friauf-type $\{T_4R_{16}\}$ tetramers, have been investigated to a lesser extent. Therefore, the band structures of prototypical compounds with $\{T_4R_{16}\}$-type tetramers, while maintaining different compositions, were analyzed employing density functional theory based methods. Furthermore, these theoretical examinations provide insight into the origin of the 15 electron rule, which is significant for this class of compounds and correlates with the closed-shell configurations for these structures. Additional research focused on the band structure of monoclinic $\{Ru_4Gd_{16}\}Br_{23}$, which is composed of rhomboid-shaped $\{Ru_4Gd_{16}\}$ tetramers.

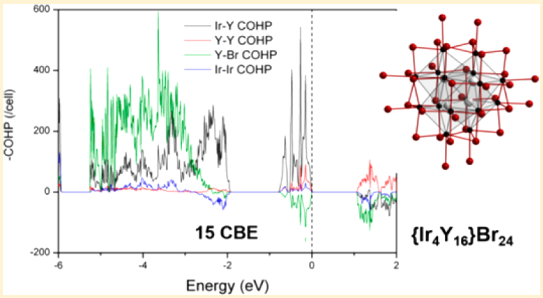

I. INTRODUCTION

Polar intermetallic compounds may be composed of polyanionic or polycationic metal atom clusters that are adjoined by monatomic counterions.[1] These are of great interest because of their outstanding structural chemistry and extensively diverse bonding regimes.[1] To provide insight into the nature of bonding for these metal atom clusters, simple electron partition rules, such as, e.g., Wade's rules[2] or the Zintl concept,[3] have emerged as a straightforward and beneficial means to identify overall bonding schemes for these compounds.[4,5] For example, the Tt^{4-} tetrahedra (Tt = Si, Ge) as seen in Na_2BaTt_4 may be depicted as two prototypical examples of Zintl anions.[6] Under consideration of more recent research,[1,7] these customary concepts seem to no longer be appropriate for an understanding of the bonding in (electron-poorer) polar intermetallic compounds.

Another prolific class of (poly)metal networks with simple counterions is the broad family of rare-earth metal (R) cluster halides (X) that encapsulate an endohedral atom (Z), from either a main group (E) or a transition metal (T).[8−14] The edges or faces as well as the vertices of these interstitially centered R cluster complexes are capped by the halido ligands (X) or, more frequently, shared with like R_r clusters to aggregate to oligomers, chains, or layers.[8,9] A series of structural families has materialized as the most prolific: (I) the $\{TR_6\}X_{12}R$ and $\{TR_6\}X_{10}$ types, with isolated $\{TR_6\}$ octahedra,[15] (II) the $\{TR_3\}X_3$ and $\{TR_4\}X_4$ types of structure, which are composed of R cluster chains encapsulating T atoms with coordination numbers of 6 and 7 ($\{TR_3\}X_3$ types) or 8 ($\{TR_4\}X_4$ type),[16−19] and (III) structures with $\{T_4R_{16}\}$ tetramers with four different compositions and structures:[20−23] the cubic $\{Mn_4Gd_{16}\}I_{24}(Gd_4I_4)$ type ($P\bar{4}3m$, No. 215),[20] two independent tetragonal structure types, first observed for $\{Ru_4Y_{16}\}I_{20}$ ($P4_2/nnm$, No. 134)[21] and $\{Ir_4Y_{16}\}Br_{24}(YBr_3)_4$ ($I4_1/a$, No. 88),[22] and the orthorhombic $\{Ir_4Y_{16}\}Br_{24}$ type (*Fddd*, No. 70).[22]

The majority of these $\{T_4R_{16}\}$-type tetramers may be depicted as two perpendicularly arranged bioctahedra, $\{T_2R_{10}\}$, condensed via four common edges to form all vertices truncated T^3 supertetrahedra, $\{T_4R_{12}{}^cR_4{}^e\}$ (e = edge-sharing R atom; c = R atoms at the corners),[20−23] in which the T atoms form a tetrahedron. There is a second type of tetramer in which the $\{T_2R_{10}\}$ bioctahedra share three common edges to aggregate to R_{16} skeletons, $\{T_4R^c{}_{10}R_6{}^e\}$, in which the four T atoms form a rhombus. This type has been observed solely for the compounds $\{B_4Tb_{16}\}Br_{23}$ and $\{Ru_4Gd_{16}\}Br_{23}$.[23,24] All structure types differ in the numbers and functionalities of

Special Issue: To Honor the Memory of Prof. John D. Corbett

Received: October 1, 2014
Published: November 20, 2014

   dx.doi.org/10.1021/ic502374y | Inorg. Chem. 2015, 54, 1026−1037

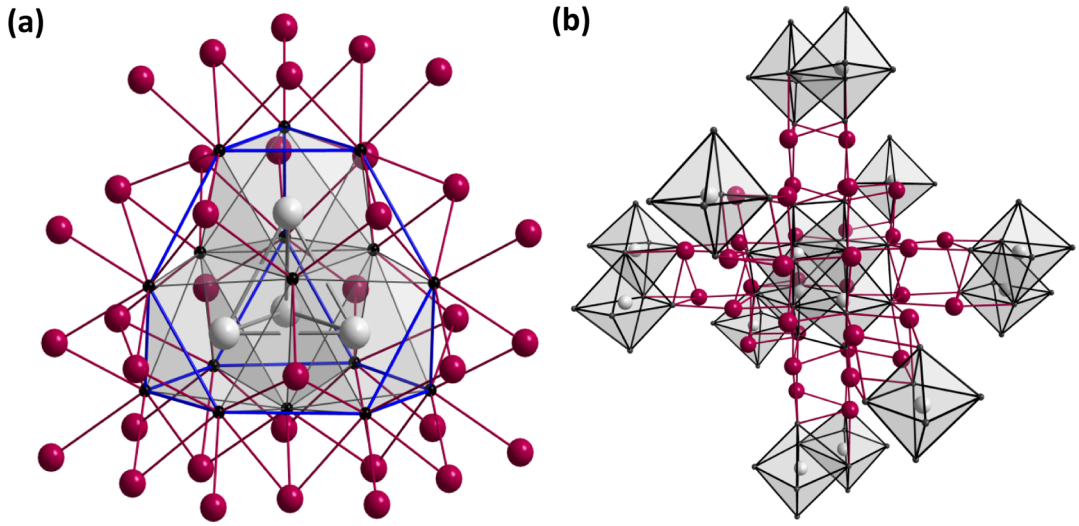

Figure 1. (a) Representation of a $\{T_4R_{12}{}^cR_4{}^e\}$ cluster oligomer (T = gray atoms; R = black atoms) surrounded by 24 inner halido ligands (purple). The tetramer may be depicted as an all-vertices truncated T3 supertetrahedron or a Friauf polyhedron. Note that the edges of all hexagonal faces are represented by blue lines. (b) Each tetramer shares 32 X atoms with eight neighboring cluster complexes (represented by cuts for a clearer illustration) via i-i, i-a, and a-i connections, respectively.

the halido ligands that interconnect the tetramers.[20−23] The incorporation of tetrahedral ($\{\square R_4\}X_4$) clusters or isolated R atoms in the voids between the $\{T_4R_{12}{}^cR_4{}^e\}$ clusters, as seen in the $\{Mn_4Gd_{16}\}I_{24}(Gd_4I_4)$-type and $\{Ir_4Y_{16}\}Br_{24}(YBr_3)_4$-type structures, adds to the structural variety of these tetrameric cluster complexes.[20,22,23]

Electron partition schemes have become apparent for the broad majority of polar intermetallic networks to recognize intracluster bonding regimes for early-transition-metal atom clusters.[8,11,25] For example, counts of 18 cluster-based electrons (CBEs), i.e., the total number of valence electrons (VEs) reduced by the number of halido ligands, still appear to be momentous for the $\{TR_6\}X_{12}R$ and $\{TR_6\}X_{10}$ types. Theoretical examinations on numerous isolated $\{TR_6\}$ clusters for both cases corroborate this simple electron counting rule.[15,26,27] However, the (electron-poorer) $\{T_tR_r\}$ clusters are rarely isolated and, more regularly, condense via common faces, edges, or (less frequent) vertices to R cluster oligomers or chains, which acquire less CBEs (often 14−17);[8,17,18] enhanced R−R bonding and less oxidation of the host T atoms are the consequence.[1] Recent explorative research on various $\{T_4R_{16}\}$ tetramers revealed a total of 15 CBEs per $\{TR_6\}$ octahedron, a meaningful count.[23] Earlier investigations on the electronic structures of tetramers such as in $\{Mn_4Sc_{16}\}Br_{24}(Sc_4Br_4)$, $\{Ru_4Sc_{16}\}Br_{24}(Sc_3Br_4)$, $\{Ru_4Y_{16}\}I_{20}$, and $\{Mn_4Gd_{16}\}I_{24}(Gd_4I_4)$ utilizing extended Hückel (EH) theory revealed closed-shell configurations for 60 CBEs per tetramer.[28] While this provides conclusive information regarding the electron counting schemes for these structure types,[28] to the best of our knowledge, the band structures of the tetragonal $\{Ir_4Y_{16}\}Br_{24}(YBr_3)_4$, the orthorhombic $\{Ir_4Y_{16}\}Br_{24}$, and monoclinic $\{Ru_4Gd_{16}\}Br_{23}$ types have yet to be analyzed.

Here we present the results of theoretical examinations on the electronic structures of prototypical examples of the $\{Ir_4Y_{16}\}Br_{24}(YBr_3)_4$, $\{Ir_4Y_{16}\}Br_{24}$, and $\{Ru_4Gd_{16}\}Br_{23}$ types of structure. As well, the band structures of members of the cubic $\{Mn_4Gd_{16}\}I_{24}(Gd_4I_4)$ and tetragonal $\{Ru_4Y_{16}\}I_{20}$ types are analyzed to extract an enhanced picture of bonding in these structure types. Crystal orbital Hamiltonian population (COHP) curves are evaluated to extract general bonding tendencies for the T-centered R tetramers.

II. COMPUTATIONAL DETAILS

More recently, density functional theory (DFT)-based methods have been shown to be advantageous instruments to provide insight into the nature of bonding for R clusters encapsulating T atoms.[15−18,29] Hence, band structure calculations were carried out for $\{Ru_4Y_{16}\}X_{20}$ (X = Br, I), $\{Ru_4Gd_{16}\}Br_{23}$, $\{Ir_4Y_{16}\}Br_{24}$, $\{Ru_4Ho_{16}\}I_{24}(Ho_4I_4)$, $\{Rh_4Tb_{16}\}Br_{24}(TbBr_3)_4$, $\{Ir_4Tb_{16}\}X_{24}(TbX_3)_4$ (X = Cl, Br), $\{Ru_4Gd_{16}\}Br_{24}(GdBr_3)_4$, and $\{T_4Sc_{16}\}Cl_{24}(ScCl_3)_4$ (T = Ru, Os, Ir) utilizing the Stuttgart tight-binding, linear muffin-tin orbital program with the atomic sphere approximation.[30−32] The Wigner−Seitz (WS) radii were automatically generated, and empty spheres were assigned in voids to guarantee an optimal approximation of full potentials. Correlation and exchange contributions were described by the local density approximation according to von Barth and Hedin.[33] The following orbitals were employed as basis sets (downfolded[34] orbitals in parentheses): Ru 5p/5s/4d/(4f); Os 6p/6s/5d/(5f); Ir 6p/6s/5d/(5f); Rh 5p/5s/4d/(4f); Sc 4p/(4s)/3d; Y 5p/(5s)/4d; Gd 6p/(6s)/5d; Tb 6p/(6s)/5d; Ho 6p/(6s)/5d (Gd, Tb, and Ho 4f states are treated as the core); Cl (4s)/3p/(3d); Br (5s)/4p/(4d); I (6s)/5p/(5d)/(4f). The corresponding WS radii [Å] were as follows: Ru, 2.79−2.88; Os, 2.90−2.91; Ir, 2.87−2.99; Rh, 2.86; Sc, 2.73−2.99; Y, 3.04−3.31; Gd, 3.07−3.38; Tb, 2.97−3.49; Ho, 3.03−3.50; Cl, 2.50−2.98; Br, 2.79−3.58; I, 3.38−3.95. Plots of the density-of-state (DOS) and −COHP curves are shown below, while projected DOS (PDOS) for the respective orbitals are provided in the Supporting Information, Figures S1−S12.

A full (chemical) bonding analysis was accomplished based on the integrated COHP (ICOHP) values. However, a direct comparison for different systems is not applicable because the electrostatic potential in each DFT-based calculation is set to an arbitrary zero energy, which can vary for various systems,[35−37] yet projecting the −ICOHP values of nearest-neighboring interactions weighed by bond frequencies as percentages of the total bonding capacities has been shown to provide conclusive information accounting for bonding differences between unlike structure types.[16,29]

III. RESULTS AND DISCUSSION

$\{Ru_4Y_{16}\}I_{20}$-Type Structures. The tetragonal $\{Ru_4Y_{16}\}I_{20}$ type of structure may be depicted as cubic closest packings of T and X atoms, with R atoms residing in $^2/_3$ of all octahedral

dx.doi.org/10.1021/ic502374y | Inorg. Chem. 2015, 54, 1026−1037

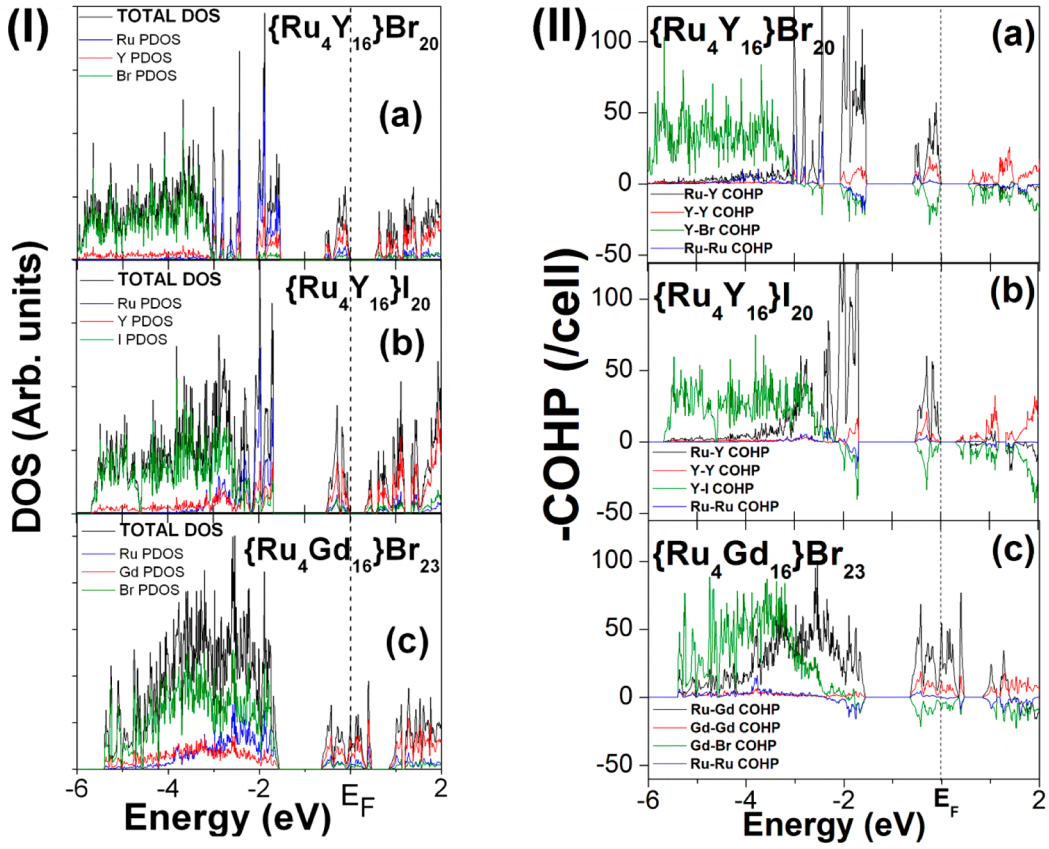

Figure 2. Plots of the various (I) DOS and (II) −COHP curves for tetragonal $\{Ru_4Y_{16}\}X_{20}$ (X = Br, I) and monoclinic $\{Ru_4Gd_{16}\}Br_{23}$.

Table 1. Distance Ranges, −ICOHP/Bond Ranges, Average −ICOHP/Bond, Cumulative −ICOHP/Cell, and Percentage Contributions for Tetragonal $\{Ru_4Y_{16}\}X_{20}$ (X = Br, I), Orthorhombic $\{Ir_4Y_{16}\}Br_{24}$, and Monoclinic $\{Ru_4Gd_{16}\}Br_{23}$[a]

	distance [Å]	−ICOHP/bond range [eV/bond]	ave −ICOHP/bond [eV/bond]	cum −ICOHP/per cell	contribution [%]
		$\{Ru_4Y_{16}\}Br_{20}$			
R−T	2.686−2.831, ⟨d⟩ = 2.752	1.47−2.56	2.03	97.38	48.8
R−R	3.535−4.458, ⟨d⟩ = 3.781	−0.01−0.20	0.11	10.38	5.2
R−X	2.890−3.134, ⟨d⟩ = 3.000	0.34−0.81	0.60	86.19	43.2
T−T	3.357−3.360, ⟨d⟩ = 3.358	0.46−0.49	0.48	5.73	2.9
		$\{Ru_4Y_{16}\}I_{20}$			
R−T	2.683−2.836, ⟨d⟩ = 2.754	1.24−2.51	1.89	90.84	50.1
R−R	3.582−4.337, ⟨d⟩ = 3.831	−0.07−0.16	0.08	8.09	4.5
R−X	3.098−3.468, ⟨d⟩ = 3.219	0.30−0.85	0.56	80.17	44.2
T−T	3.571−3.572, ⟨d⟩ = 3.571	0.18−0.18	0.18	2.18	1.2
		$\{Ir_4Y_{16}\}Br_{24}$			
R−T	2.724−2.833, ⟨d⟩ = 2.789	1.66−2.42	2.03	429.81	41.9
R−R	3.590−4.540, ⟨d⟩ = 3.824	−0.01−0.16	0.08	36.09	3.5
R−X	2.790−3.144, ⟨d⟩ = 2.936	0.33−1.27	0.80	530.95	51.8
T−T	3.294−3.328, ⟨d⟩ = 3.315	0.58−0.63	0.60	28.87	2.8
		$\{Ru_4Gd_{16}\}Br_{23}$			
R−T	2.685−2.869, ⟨d⟩ = 2.757	1.93−2.81	2.48	118.83	47.3
R−R	3.661−4.481, ⟨d⟩ = 3.863	0.03−0.20	0.13	12.63	5.0
R−X	2.828−3.090, ⟨d⟩ = 2.980	0.46−1.23	0.79	114.21	45.5
T−T	3.403−3.697, ⟨d⟩ = 3.599	0.33−0.68	0.45	5.36	2.1

[a]Details of the crystal structures have been reported elsewhere.[21−23]

voids. Thereby R atoms occupy the holes surrounding the T atoms and, accordingly, aggregate to $\{T_4R_{12}{}^cR_4{}^e\}$-type tetramers, which are enclosed by 36 halido ligands. The 24 inner X^i ligands cap 12 faces and 12 edges of one tetramer in a μ_3 and μ_2 fashion, respectively, while the 12 outer μ_1-X^a ligands reside in the inner coordination sphere of neighboring tetramers. The outer as well as 20 of the inner halido ligands of one tetramer are shared with eight neighboring tetramers via i-i, i-a, and a-i connections (Figure 1). In summary, all functionalities identified in the $\{Ru_4Y_{16}\}I_{20}$-type structures can be represented by the formula $\{T_4R_{16}\}X_4{}^iX_{8/2}{}^{i\text{-}i}X_{12/2}{}^{i\text{-}a}X_{12/2}{}^{a\text{-}i}$ =

dx.doi.org/10.1021/ic502374y | Inorg. Chem. 2015, 54, 1026−1037

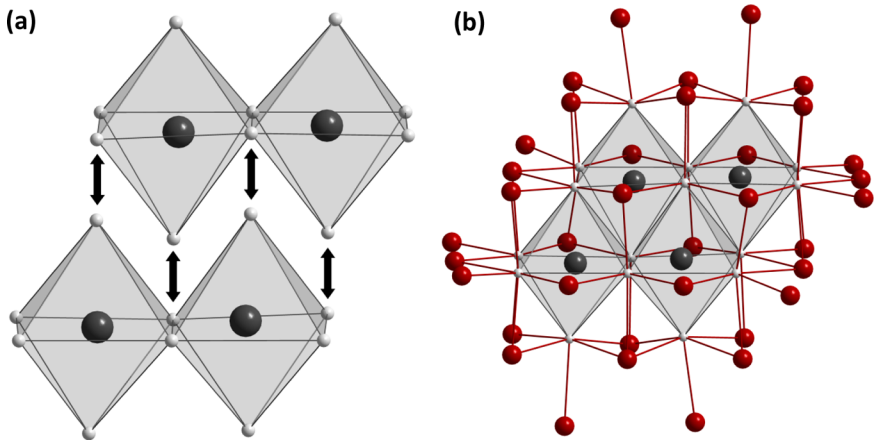

Figure 3. (a) Representation of a rhomboid-shaped $\{T_4R^c{}_{10}R_6^e\}$-type tetramer (T = black atoms; R = gray atoms), as seen in monoclinic $\{Ru_4Gd_{16}\}Br_{23}$ (details of the crystal structure have been reported elsewhere[23]). (b) Each tetramer is enclosed by 36 halido ligands (X = red atoms).

$\{T_4R_{16}\}X_{20}$. The tetragonal $\{Ru_4Y_{16}\}I_{20}$ type has, as of today, been observed solely for group eight interstitials.[23]

Analysis of the DOS curves [Figure 2(I)-a,b] for the tetragonal $\{Ru_4Y_{16}\}I_{20}$ structure reveals that significant contributions from I 5p atomic orbitals (AOs) reside in the vicinity of the Y 4d and Ru 4d states (between −3.31 and −1.68 eV), yet in the Br-containing structure, the Br 4p states (below −2.94 eV) have moved mostly beneath considerable Y 4d and Ru 4d states (between −3.04 and −1.53 eV) because of the rather high electron affinity of Br. Note that these Y 4d and Ru 4d states exhibit smaller dispersions than those for the halide states. Below E_F, there is a broad gap between −1.53 and −0.61 eV for tetragonal $\{Ru_4Y_{16}\}Br_{20}$ and between −1.68 and −0.52 eV for the isostructural I-containing $\{Ru_4Y_{16}\}I_{20}$. Examinations of the DOS regions between these gaps and the Fermi level, E_F, for both compounds show that these states stem largely from the Y 4d states with minor contributions from the Ru 5p AOs. Integrating these energy regions of the DOS curves for both cases makes plain that there are six states per formula unit (f.u.), which may be assigned to the $\{Ru_4Y_{16}\}$ cluster-based orbitals.[28] Because of a gap between E_F and +0.54 eV for $\{Ru_4Y_{16}\}Br_{20}$ and E_F and +0.29 eV for $\{Ru_4Y_{16}\}I_{20}$, an activated conductivity is suggested for both structures. Actually, a closed-shell configuration has been proposed previously for $\{Ru_4Y_{16}\}Br_{20}$ because temperature-independent van Vleck paramagnetism was observed for a temperature range from 50 to 300 K.[22]

In brief, analysis of the DOS curves for both structures infers the paramount role of heteroatomic T−R and R−X bonding. Analysis of the −COHP curves [Figure 2(II)-a,b] provides an enhanced bonding picture.

In the case of tetragonal $\{Ru_4Y_{16}\}Br_{20}$, significant Ru−Y bonding interactions reside between −3.04 and −1.53 eV (Figure 2), whereas sizable Ru−Y bonding interactions range from −3.31 to −1.68 eV for the analogous iodide. Additionally, the Y−X interactions change from bonding to antibonding at −3.04 eV for $\{Ru_4Y_{16}\}Br_{20}$ and −2.10 eV for the isostructural iodide; hence, the occupation of antibonding Y−X states (X = Br, I) at such low energy may be regarded as conclusive evidence for a less bonding character relative to the Y−Ru bonds, yet for tetragonal $\{Ru_4Y_{16}\}X_{20}$ (X = Br, I), the Y−X −ICOHP values range from 0.34 to 0.81 eV/bond for X = Br and from 0.30 to 0.85 eV/bond for X = I. Comparatively, the Ru−Y −ICOHP values vary between 1.46 and 2.56 eV/bond for $\{Ru_4Y_{16}\}Br_{20}$ and between 1.24 and 2.51 eV/bond for $\{Ru_4Y_{16}\}I_{20}$ (Table 1). Because these values contribute 48.8% (Y−Ru; X = Br), 50.1% (Y−Ru; X = I), 43.2% (Y−Br), and 44.2% (Y−I) to the total −ICOHP, these (heteroatomic) interactions should be deliberated as the essential bonding network of these structures. Taking more recent theoretical investigations on R cluster compounds into account,[16,29] the Ru−Y interactions may be exemplified in Brewer's sense of polar intermetallic bonding interactions.[38] However, for tetragonal $\{Ru_4Y_{16}\}X_{20}$ (X = Br, I), Y−Y −ICOHP values reach from −0.01 to 0.20 eV/bond for X = Br and from −0.01 to 0.16 eV/bond for X = I. Notwithstanding that Y−Y bonding is a structural factor, the moderate share of Y−Y interactions (5.2% for X = Br and 4.5% for X = I) to the total −ICOHP indicate that the Y−Y interactions play a minor, but evident, role in the overall bonding. Hence, the results thereof denote that the conventional means of delineating clusters as anticipated by Cotton[39] do not, strictly speaking, apply to $\{Ru_4Y_{16}\}$ tetramers.

$\{Ru_4Gd_{16}\}Br_{23}$. This structure is composed of $\{T_4R^c{}_{10}R_6^e\}$-type tetramers, which stem from the condensation of two dimers, $\{T_2R_{10}\}$, via three common edges (Figure 3). Gd atoms that surround the Ru interstitials reside in $^{16}/_{27}$ of all octahedral holes comprised by the cubic closest packing of Ru and Br atoms. Each tetramer is surrounded by 36 bromide ligands, which partially connect one tetramer with neighboring $\{Ru_4Gd^c{}_{10}Gd_6^e\}$ clusters according to $\{Ru_4Gd_{16}\}Br_{12}{}^{i}Br_{10/2}{}^{i\text{-}i}Br_{4/2}{}^{i\text{-}a}Br_{4/2}{}^{a\text{-}i}Br_{6/3}{}^{a\text{-}a\text{-}a}$.

The DOS [Figure 2(I)-c] of monoclinic $\{Ru_4Gd_{16}\}Br_{23}$ shows a distinctly different electronic structure relative to the tetragonal $\{Ru_4Y_{16}\}I_{20}$-type structures. In particular, in the case of the monoclinic structure, significant Gd 5d and Ru 4d states lie in the same energy regions of the DOS curves as the Br 4p states. Below E_F, a broad gap opens between −0.64 and −1.56 eV, while the energy regions of the DOS near E_F arise from the Gd 5d AOs with minor contributions from the Ru 5p AOs. A clear distinction in this DOS curve from those for the tetragonal structures occurs at the Fermi level; E_F is placed at a peak of the DOS, suggesting metallic behavior of monoclinic $\{Ru_4Gd_{16}\}Br_{23}$, yet the small dispersion of this band is indicative for low electronic mobility and rather localized states. Below that peak, a conspicuous pseudogap is generated for the DOS region of electron counts of 193−195 VE.

Analysis of the −COHP curves [Figure 2(II)-c] for monoclinic $\{Ru_4Gd_{16}\}Br_{23}$ reveals that heteroatomic Ru−Gd

dx.doi.org/10.1021/ic502374y | Inorg. Chem. 2015, 54, 1026−1037

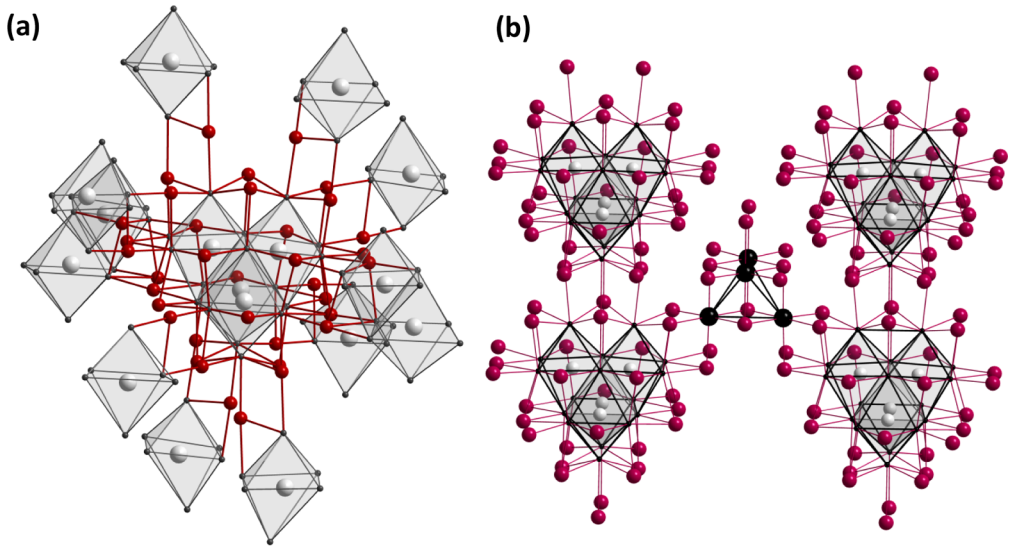

Figure 4. (a) $\{Ir_4Y_{16}\}Br_{36}$ unit as it appears in orthorhombic $\{Ir_4Y_{16}\}Br_{24}$ (Ir = gray atoms; Y = black atoms; Br = red atoms).[22] Sections of the 10 nearest-neighboring clusters are denoted. (b) Representation of a (R_4X_4) cluster complex surrounded by $\{T_4R_{16}\}X_{36}$ tetramers as seen in cubic $\{Ru_4Ho_{16}\}I_{24}(Ho_4I_4)$.[23]

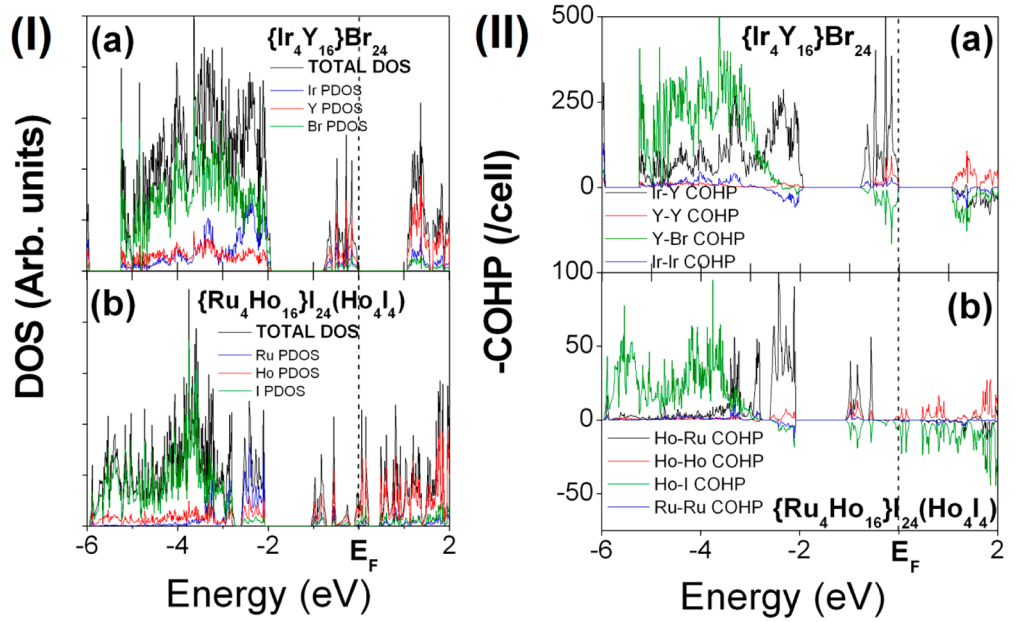

Figure 5. Plots of the various (I) DOS and (II) −COHP curves for orthorhombic $\{Ir_4Y_{16}\}Br_{24}$ and cubic $\{Ru_4Ho_{16}\}I_{24}(Ho_4I_4)$. The Fermi level, E_F, is represented by dotted lines.

and Gd−Br interactions dominate above minor, but evident, homoatomic interactions. Reasonable Gd−Gd bonding interactions reside between −0.64 eV and E_F; Gd−Gd −ICOHP values range between 0.03 and 0.20 eV/bond and contribute 5.0% to the total bonding capacities (Table 1). Hence, such relatively minor interactions between the Gd atoms indicate that the bonding network should not be illustrated in Cotton's sense of transition-metal atom clusters.[39] A close inspection of the band structure for monoclinic $\{Ru_4Gd_{16}\}Br_{23}$ reveals that the Fermi level is placed at a peak of the DOS above a notable pseudogap, which typically designates an electronically unfavorable situation, yet integrating the energy regions between two pseudogaps at −0.08 eV (∼194 VEs) and 0.09 eV (∼196 VEs) reveals that there is one state per f.u. near E_F that can be assigned to a singly occupied cluster-based (HO)MO. It is possible that monoclinic $\{Ru_4Gd_{16}\}Br_{23}$ may alleviate its electronic instability by structural distortions, i.e., substantial deviations from the ideal O_h symmetry within the $\{RuGd_6\}$ octahedra.[23]

$\{Ir_4Y_{16}\}Br_{24}$. This structure has been previously reported to crystallize with the orthorhombic space group *Fddd* (No. 70) and is also composed of $\{T_4R_{12}{}^cR_4{}^e\}$-type tetramers (Figure 4).[22] Each $\{Ir_4Y_{16}\}$ tetramer is encased by 24 inner bromido ligands capping 12 edges and 12 faces in a μ_2- and μ_3-like manner, respectively. The 12 outer Br^a ligands reside in the inner coordination spheres of 10 nearest-neighboring tetramers and, in reply, 12 inner bromido ligands, Br^i, connect each $\{Ir_4Y_{16}\}$ cluster with 10 like tetramers via i-a bonds. All functionalities may be depicted by $\{Ir_4Y_{12}{}^cY_4{}^e\}$-$Br_{12}{}^iBr_{12/2}{}^{i\text{-}a}Br_{12/2}{}^{a\text{-}i}$ = $\{Ir_4Y_{16}\}Br_{24}$. To the best of our

dx.doi.org/10.1021/ic502374y | Inorg. Chem. 2015, 54, 1026−1037

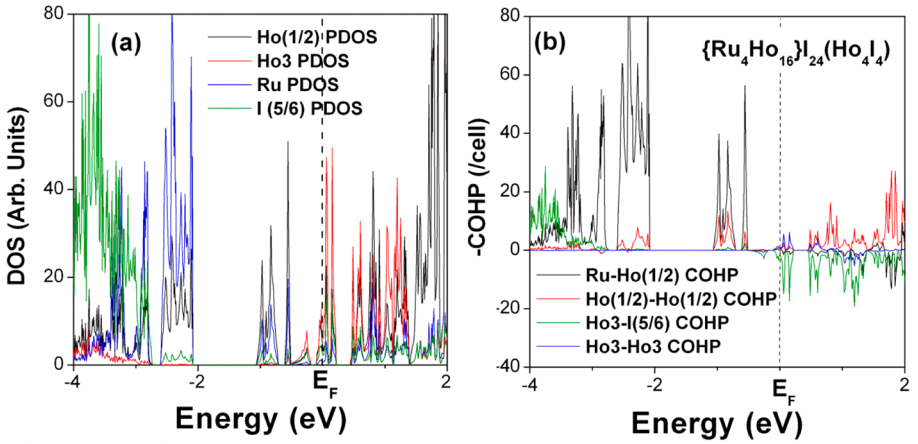

Figure 6. (a) Plots of the PDOS for the cluster-based Ho(1/2), endohedral Ru, isolated Ho3, and I(5/6) sites. (b) −COHP curves for the cluster-based Ru−Ho(1/2) (black) as well as Ho(1/2)−Ho(1/2) interactions (red). The Ho3−I(5/6) and Ho3−Ho3 interactions are represented by the green and blue −COHP curves, respectively. The Fermi level is denoted by dotted lines.

knowledge, this type of structure has been observed solely for $\{Ir_4Y_{16}\}Br_{24}$.

An examination of the DOS curves for orthorhombic $\{Ir_4Y_{16}\}Br_{24}$ [Figure 5(I)-a] unveils that the Ir 5d, Y 4d, and Br 4p states fall below a broad gap ranging from −1.93 to −0.79 eV. States near E_F emanate from the Y 4d AOs with minor contributions from Ir 6p AOs. Additionally, these regions of the DOS comprise six states per f.u., which can be assigned to the (a_1-, e-, and t-type) cluster orbitals.[28] Note that the states near E_F exhibit a modest dispersion relative to the remaining states. Because of a gap between E_F and +1.07 eV, an activated conductivity is suggested for the orthorhombic structure, yet the conductivity has not been measured for that structure.

A bonding analysis based on the −COHP curves [Figure 5(II)-a] for that structure indicates that momentous Ir−Y bonding interactions are located below −1.93 eV and between −0.79 eV and E_F. As Y−Br interactions cross from bonding to antibonding states at −2.35 eV, a less bonding character of the Y−Br interactions can be deduced relative to the Ir−Y states. Also, the heteroatomic Y−Br and Ir−Y interactions contribute 51.8% and 41.9%, respectively (Table 1), to the total −ICOHP and, accordingly, may be regarded as the paramount bonding contributions in orthorhombic $\{Ir_4Y_{16}\}Br_{24}$. Y−Y interactions play a subordinate role in the overall bonding because these states contribute 3.5% to the total −ICOHP. In view of the fact that the −ICOHP values are inclined to correlate well with the bond strength, the magnitudes of the −ICOHP values will tend to diminish as the bond lengths increase. Hence, the T−T distances in all structures range from 3.294 to 3.697 Å and, consequently, exhibit modest contributions to the total −ICOHP (Table 1).

In summary, analyzing the DOS and −COHP curves for the tetragonal $\{Ru_4Y_{16}\}X_{20}$ (X = Br, I), orthorhombic $\{Ir_4Y_{16}\}Br_{24}$, and monoclinic $\{Ru_4Gd_{16}\}Br_{23}$ structures reveals that the overall bonding is dominated by heteroatomic T−R and R−X interactions, whereas homoatomic R−R and T−T bonding plays a subordinate role. Particularly, the T−R interactions should be contemplated as polar intermetallic bonds, as anticipated by Brewer.[38] Additionally, the states near E_F show modest dispersions and may be assigned to the tetramer-based orbitals.[28] In the case of the tetragonal and orthorhombic structures, E_F falls in a gap, which typically signifies electronic stability. In the monoclinic structure, however, E_F is placed on a maximum of the DOS, which may be regarded as an electronically unfavorable situation. Although these investigations on the electronic structures of a series of $\{T_4R_{12}{}^cR_4{}^e\}$-type tetramers provided insight into the (general) nature of bonding for these structures and, of greater consequence, the origin of the "15-electron-rule", they cannot account for the existence of compounds that comprise $\{T_4R_{12}{}^cR_4{}^e\}$-type tetramers.

$\{Ru_4Ho_{16}\}I_{24}(Ho_4I_4)$. This compound crystallizes with the cubic $\{Mn_4Gd_{16}\}I_{24}(Gd_4I_4)$-type ($P\bar{4}3m$, No. 215) and also contains $\{T_4R_{12}{}^cR_4{}^e\}$-type tetramers (Figure 4b). In particular, the cubic structure contains three independent Ho sites [Wyckoff 4e (Ho1), 12i (Ho2), and 4e (Ho3)], three I sites [Wyckoff 12i (I4), 12i (I5), and 4e (I6)], and one Ru site (Wyckoff 4e). Each endohedral Ru atom is surrounded by three Ho1 and three Ho2 atoms, such that the Ho1 atoms occupy the centers of the hexagonal faces of the Friauf-type polyhedron, with Ho2 atoms residing on its vertices. Additionally, 12 faces of each tetramer are μ_3-capped by the I4 ligands, which also interconnect one cluster with six nearest-neighboring tetramers via i-a functionalities. In response, the outer μ_1-I4 ligands are located in the inner coordination spheres of six like tetramers and, hence, possess a-i functionalities. However, the I5 ligands cap 12 edges of each tetramer in a μ_2-like fashion and bond to the (*exo*-)Ho3 atoms, which form $\{\square(Ho3)_4\}$ tetrahedra. The voids of these $\{\square(Ho3)_4\}$ clusters are empty, while the triangular faces of each tetrahedron are capped by the I6 atoms in a μ_3-like manner. Note that these isolated $\{\square(Ho3)_4\}(I6)_4$ clusters are isostructural with those observed for binary PrI_2−V.[40,41] In summary, all functionalities identified for cubic $\{Ru_4Ho_{16}\}I_{24}(Ho_4I_4)$ may be represented by $\{Ru4\text{-}(Ho1)^e{}_4(Ho2)^c{}_{12}\}(I5)^{i\text{-}t}{}_{12}(I4)^{i\text{-}a}{}_{12/2}(I4)^{a\text{-}i}{}_{12/2}(\{\square(Ho3)_4\}(I6)^i{}_4)$ (the superscript "t" represents the connection from I5 atoms to the $\{\square(Ho3)\}$ tetrahedra).

Previous research on a series of cubic $\{Mn_4Gd_{16}\}I_{24}(Gd_4I_4)$-type tetramers, which are $\{T_4Sc_{16}\}Br_{24}(Sc_4Br_4)$ (T = Mn, Fe, Ru, Os), was analyzed employing EH theory.[28] The isolated R3 atom sites in these structures were shown to possess partial occupancies, which were considered to refine the CBE counts. Actually, the total number of 60 (skeletal) electrons per tetramer was shown to correspond to the closed-shell configurations for these structures.[28] Additionally, analysis of the various DOS and −COHP curves for tetragonal $\{Ru_4Y_{16}\}X_{20}$ (X = Br, I) and orthorhombic $\{Ir_4Y_{16}\}I_{24}$ with (formally) 15

dx.doi.org/10.1021/ic502374y | Inorg. Chem. 2015, 54, 1026−1037

Table 2. Distance Ranges, −ICOHP/Bond Ranges, Average −ICOHP/Bond, Cumulative −ICOHP/Cell, and Percentage Contribution for Cubic $\{Ru_4Ho_{16}\}I_{24}(Ho_4I_4)$[a]

	distance [Å]	−ICOHP/bond range [eV/bond]	ave −ICOHP/bond [eV/bond]	cum −ICOHP/per cell	contribution [%]
		$\{Ru_4Ho_{16}\}I_{24}(Ho_4I_4)$			
Ru−Ho	2.692−2.805, ⟨d⟩ = 2.749	1.46−2.58	2.02	48.52	39.0
Ho−Ho	3.594−4.455, ⟨d⟩ = 3.876	−0.03−0.19	0.09	5.06	4.1
Ho−I	3.134−3.484, ⟨d⟩ = 3.200	0.28−1.212	0.71	68.32	54.9
Ru−Ru	3.458	0.42	0.42	2.50	2.0

[a]Details of the crystal structure have been reported elsewhere.[23]

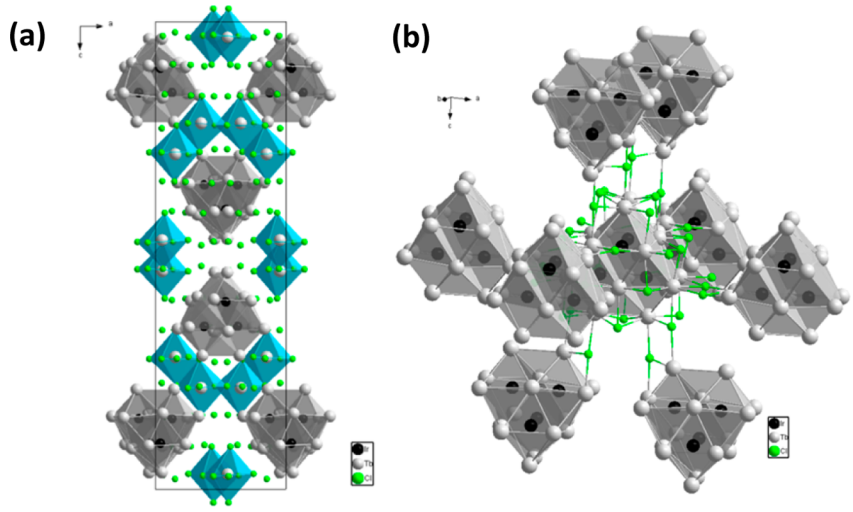

Figure 7. (a) Unit cell of $\{Ir_4Tb_{16}\}Cl_{24}(TbCl_3)_4$ with $\{Ir_4Tb_{16}\}$ tetramers (gray) and chains of $[TbCl_3]$ units (blue). (b) Representation of a $\{T_4R_{16}\}$-type tetramer surrounded by 36 halido ligands and its 8 nearest-neighboring clusters.

CBEs indicated that E_F falls in a broad gap, which typically indicates electronic stability. However, partial occupancies have not been observed for the (isolated) Ho3 sites in cubic $\{Ru_4Ho_{16}\}I_{24}(Ho_4I_4)$ and, thus, this structure appears to withstand the "15-electron-rule".[23] To elucidate the bonding regimes for this structure, we followed up with analysis of the DOS and −COHP curves for cubic $\{Ru_4Ho_{16}\}I_{24}(Ho_4I_4)$ [Figure 5(I)-b,(II)-b].

Analysis of the DOS curves for the cubic structure shows that significant I 5p, Ru 4d, and Ho 5d states are located below a broad gap, which ranges from −2.08 to −1.07 eV. A close inspection of the bands residing between −1.07 and −0.51 eV reveals that these states arise from the Ru 5p AOs with reasonable contributions from the (cluster-based) Ho(1/2) 5d AOs. Integrating these energy regions of the DOS curves discloses that there are six states per f.u., which may be assigned to the tetramer-based orbitals.[28] Additionally, these states also exhibit a smaller dispersion relative to the I states and correspond to VE counts of 216−228, which is a guide to a total of 60 CBEs per tetramer. However, the states near E_F originate mostly from the Ho3 AOs with notable shares with I(5/I6) AOs (Figure 6). Because E_F falls in a local minimum of the DOS curve for VE counts of 232−234, an (electronically) favorable situation can be inferred for cubic $\{Ru_4Ho_{16}\}I_{24}(Ho_4I_4)$.

Again, an examination of the DOS curves for the cubic $\{Ru_4Ho_{16}\}I_{24}(Ho_4I_4)$ structure indicates that this structure gains significant stabilization from heteroatomic Ho−Ru and Ho−I bonding. Moreover, an (electronically) favorable closed-shell configuration has been identified for the $\{Ru_4Ho_{16}\}$ tetramers, while states near E_F stem from the (*exo*-)Ho3−I(5/6) interactions, yet an enhanced picture of bonding may be extracted from analysis of the −COHP curves for that structure.

In the cubic $\{Ru_4Ho_{16}\}I_{24}(Ho_4I_4)$ structure, the various −COHP curves [Figures 5(**II**)-b and 6b] and −ICOHP values (Table 2) are evidence for modest Ho−Ho bonding and strong Ru−Ho interactions below E_F. Heteroatomic Ho−Ru interactions contribute 39.0% to the total −ICOHP, while the Ho−Ho −ICOHP values range between −0.03 and 0.19 eV/bond and add 4.1% to the total bonding capacities. Accordingly, such relatively minor Ho−Ho and major Ho−Ru interactions indicate that the bonding situation in these tetramers should be depicted in Werner's sense of coordination networks rather than in Cotton's traditional conception.[8,39] Additionally, the Ho−I interactions traverse from bonding to antibonding states at −2.83 eV, and, accordingly, the occupation of antibonding Ho−I states at such low energies may be regarded as conclusive evidence for less bonding character relative to the Ho−Ru interactions. Note that minor, but evident, Ho3−Ho3 bonding interactions are evident around E_F; however, the −ICOHP values of 0.01 eV/bond for the Ho3−Ho3 interactions (d = 4.455 Å) suggest only modest bonding interactions for these contacts. Notably, integrations of the PDOS across all Ho sites indicate that the Ho3 sites are the less electron-deficit metal sides ("less oxidized"). Hence, a (formal) electron partition scheme bordering on 15 + 1 CBEs appears more appropriate to depict the overall bonding situation for the cubic $\{Ru_4Ho_{16}\}I_{24}(Ho_4I_4)$ structure, which was also shown to follow the "15-electron-rule".

$\{Ir_4Y_{16}\}Br_{24}(YBr_3)_4$-Type Structures. The tetragonal $\{Ir_4Y_{16}\}Br_{24}(YBr_3)_4$ type of structure may be depicted as cubic closest packing of T and X atoms, with R atoms residing

dx.doi.org/10.1021/ic502374y | Inorg. Chem. 2015, 54, 1026−1037

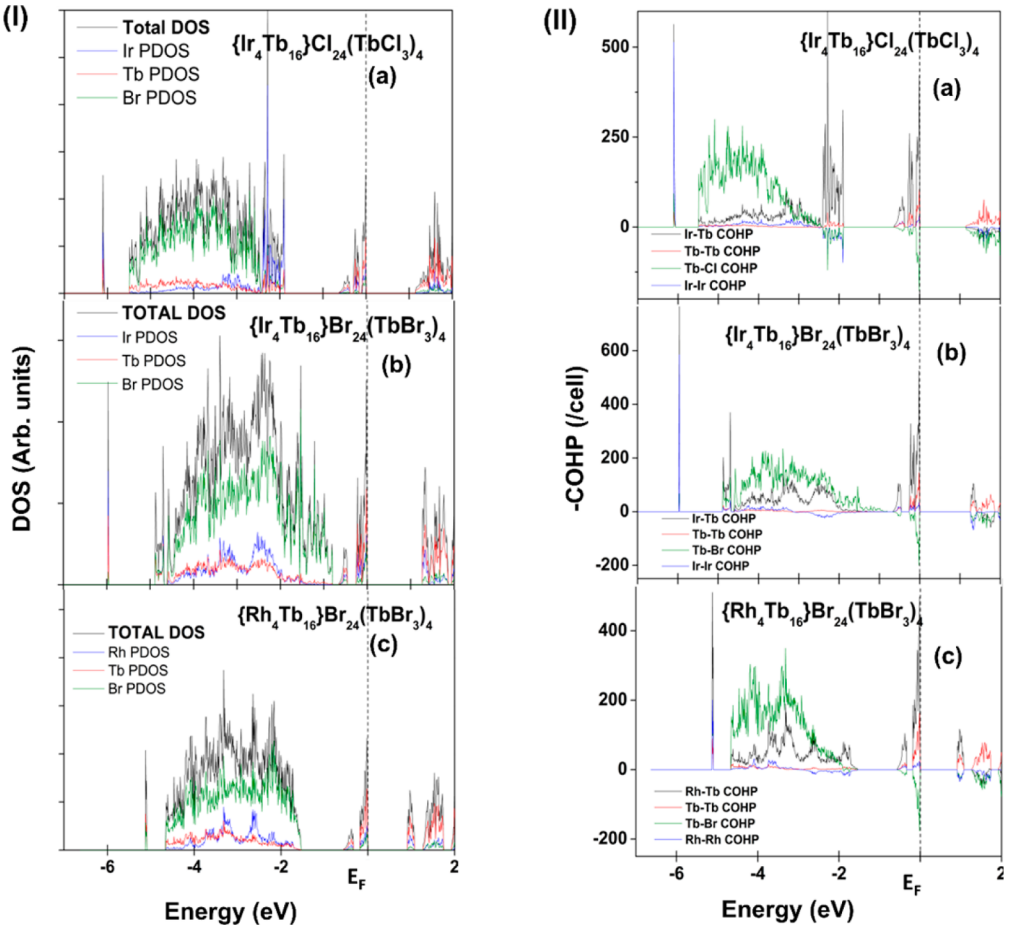

Figure 8. Plots of the various (I) DOS and (II) −COHP curves for prototypical $\{T_4R_{16}\}X_{24}(RX_3)_4$-type compounds. The Fermi level, E_F, is represented by dotted lines.

in $^1/_2$ of all octahedral voids. More specifically, $^4/_5$ of all R atoms occupy those holes surrounding the T atoms to aggregate to $\{T_4R_{12}{}^cR_4{}^e\}$-type tetramers (Figure 7b), which are surrounded by 36 halido ligands: 24 inner halido ligands, X^i, capping 12 faces and 12 edges of one tetramer in μ_3 and μ_2 fashion, respectively, and 12 outer μ_1-X^a ligands. In particular, eight of the X^a ligands reside in the inner coordination spheres of eight nearest-neighboring tetramers, forming a-i connections. In reverse, eight of the X^i ligands of each tetramer belong to the outer coordination spheres of the eight nearest-neighboring tetramers and, thus, possess i-a functionalities. Because of this, square cluster networks of ligand-linked tetramers are formed within the *ab* plane and a pseudotetrahedral connection of five tetrameric clusters is generated along the crystallographic *c* axis (Figure 7a).

Above all, $^1/_5$ of all R atoms reside in octahedral voids formed by six X atoms, $[RX_6]$: one μ_2-X^i ligand and one X^a ligand of one nearest-neighboring tetramer, $X^{a/i\text{-}ch}$ (the superscript ch represents $X^{i/a}$ ligands bonding to the $[RX_6]$ unit chains) and four discrete halide atoms, X^{ch} and X^{cl} (the superscript cl represents X^{ch} atoms bonding to the clusters). More specifically, these $[RX_6]$ octahedra are edge-condensed to form zigzag chains, which run alternately along the *a* and *b* axes between the cluster networks within the *ab* plane (Figure 7a). All functionalities can be represented by $\{T_4R_{16}\}$-$X_{12}{}^iX_{8/2}{}^{i\text{-}a}X_{4/2}{}^{i\text{-}ch}X_{8/2}{}^{a\text{-}i}X_{4/2}{}^{a\text{-}ch}{\cdot}4RX_{4/2}{}^{ch}X_{2/2}{}^{cl}$.

Analysis of the DOS curves for tetragonal $\{T_4Sc_{16}\}$-$Cl_{24}(ScCl_3)_4$ (T = Ru, Ir, Os), $\{Ru_4Gd_{16}\}Br_{24}(GdBr_3)_4$, $\{Ir_4Tb_{16}\}Cl_{24}(TbCl_3)_4$, and $\{T_4Tb_{16}\}Br_{24}(TbBr_3)_4$ (T = Rh, Ir) reveals significant contributions from the R s and T s bands corresponding to narrow peaks residing below the X p states. The positions of these peaks relative to the X p states vary for each system because of the diverse effective nuclear charges of the endohedral atoms and the corresponding rare-earth metals, such as, e.g., Ru vs Os [Figure 9(I)-b,c], Rh vs Ir [Figure 8(I)-b,c], and Sc vs Tb [Figures 9(I)-a and 8(I)-a]. Additionally, these maxima of the DOS curves are well separated from the X p states through band gaps from 0.13 to 1.1 eV, whereas the X p states reside mostly between −5.48 and −1.88 eV for the chlorides and between −4.88 and −0.80 eV for the isostructural bromides (see Figures 8 and 9). These bands derive mainly from the X p states with minor contributions from the R d and R s AOs. Notably, the energy regions of the X p bands for the chloride are lower in energy than those for the isostructural bromide [e.g., $\{Ir_4Tb_{16}\}Cl_{24}(TbCl_3)_4$ vs $\{Ir_4Tb_{16}\}Br_{24}(TbBr_3)_4$; Figure 8(I)-a,b] because of an increased electron affinity from Br to Cl.

A close inspection of the energy regions near the X p bands for all tetragonal $\{T_4R_{16}\}X_{24}(RX_3)$-type structures reveals that there are two maxima within the partial T DOS arising from T d bands. Furthermore, the relative positions of these T d bands are affected by magnitudes of the effective nuclear charges of T. For instance, these bands range from −2.13 to −1.44 eV for the tetragonal $\{Os_4Sc_{16}\}Cl_{24}(ScCl_3)_4$ and from −2.90 to −1.87 eV for the isostructural Ir-containing compound because of an increased electron affinity from Os to Ir. Moreover, these X p

dx.doi.org/10.1021/ic502374y | Inorg. Chem. 2015, 54, 1026−1037

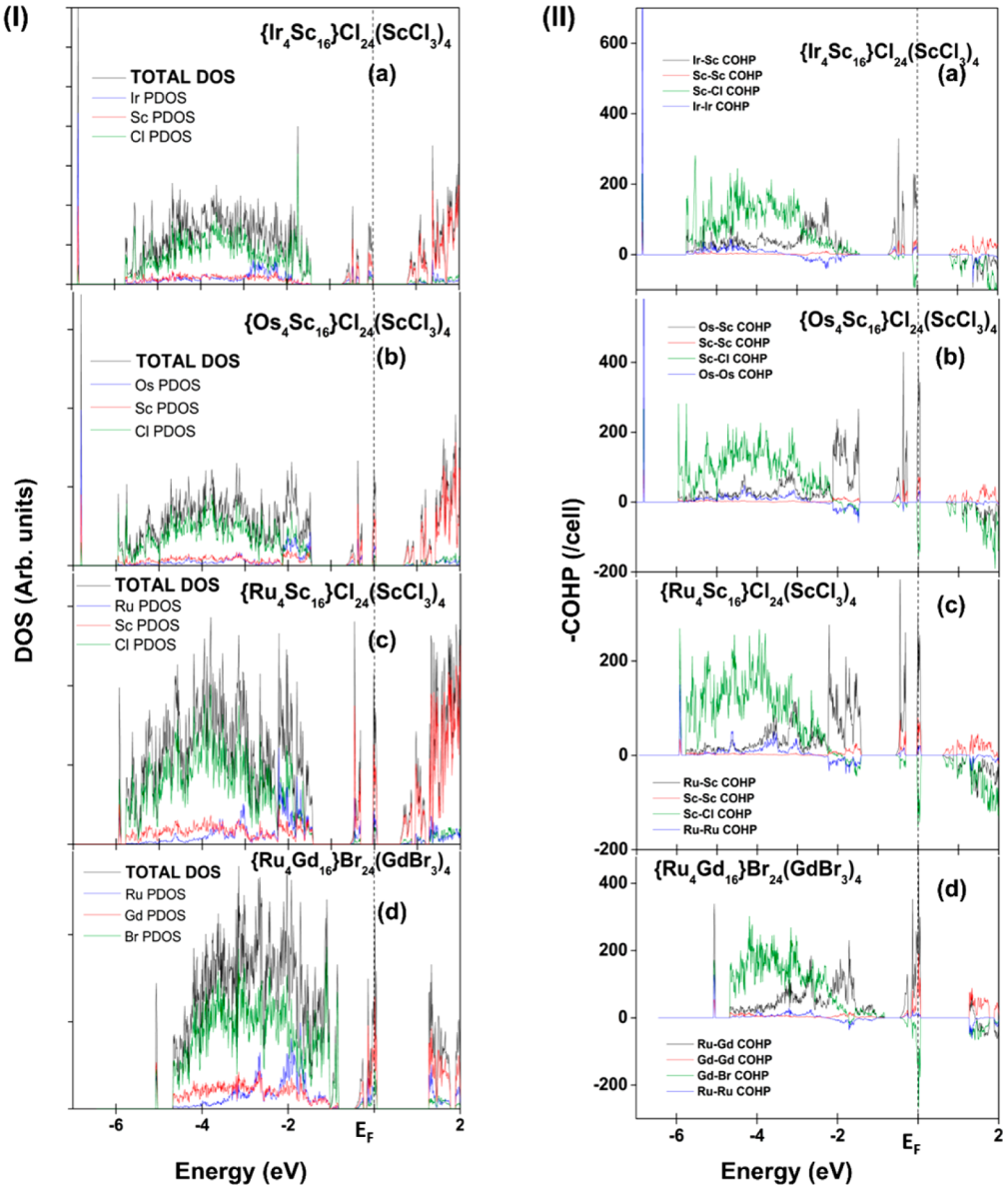

Figure 9. Plots of the various (I) DOS and (II) −COHP curves for tetragonal $\{T_4Sc_{16}\}X_{24}(ScX_3)_4$ (T = Ru, Os, Ir) and $\{Ru_4Gd_{16}\}Br_{24}(GdBr_3)_4$. The Fermi level, E_F, is represented by dotted lines.

and T d bands are clearly segregated from the states near E_F by broad gaps (see Figures 8 and 9), whose relative sizes tend to correlate to the magnitude of the electron affinities of X ligands and the endohedral T atoms. For instance, there is a smaller band gap (between −0.79 and −0.61 eV) in $\{Ir_4Tb_{16}\}Br_{24}(TbBr_3)_4$ rather than in $\{Ir_4Tb_{16}\}Cl_{24}(TbCl_3)_4$ [between −1.88 and −0.62 eV; see Figure 8(I)-a,b]. The energy regions of the DOS curves near E_F stem mostly from R d states with minor contributions from X p and T p AOs. Integrating these energy regions of the DOS curves reveals that there are six states per f.u. that correspond to cluster-based MOs. Note that the states near E_F exhibit relatively small dispersions, which typically indicates localized states.

Even though the gross features of the DOS near E_F are analogous for all $\{T_4R_{16}\}X_{24}(RX_3)$-type compounds, they vary in the number of VEs. In particular, E_F falls in a gap in compounds with group 9 interstitials (15 CBEs), whereas E_F in compounds with group 8 endohedral atoms (14 CBEs) falls in a peak below that gap. Accordingly, counts of 15 CBEs result in closed-shell configurations with band gaps from 0.80 to 1.27 eV above the Fermi level. The different positions of E_F suggest potentially dissimilar conductivities for compounds with group 9 interstitials, which should be semiconductors, and compositions with group 8 interstitials, which should be metallic. However, the small dispersions of the states near E_F are commonly indicative for low electron mobility, which more likely implies the existence of localized electronic states rather than metallic character.

Detailed analysis of the various −COHP curves for the tetragonal structures shows a bonding situation similar to that for other T-centered R cluster halides:[15−18] the heteroatomic R−X and R−T interactions predominate homoatomic R−R and T−T interactions. Still, T−T bonds are important for structural distortions ("breathing distortion"). To analyze this outcome in more detail, we follow up with an analysis of the −COHP curves for tetragonal $\{T_4R_{16}\}X_{24}(RX_3)$-type structures.

dx.doi.org/10.1021/ic502374y | Inorg. Chem. 2015, 54, 1026−1037

Table 3. Distance Ranges, −ICOHP/Bond Ranges, Average −ICOHP/Bond, Cumulative −ICOHP/Cell, and Percentage Contributions for Tetragonal $\{Ir_4Tb_{16}\}X_{24}(TbX_3)_4$ (X = Cl, Br) and $\{Rh_4Tb_{16}\}Br_{24}(TbBr_3)_4$[a]

	distance [Å]	−ICOHP/bond range [eV/bond]	ave −ICOHP/bond [eV/bond]	cum −ICOHP/per cell	contribution [%]
		$\{Ir_4Tb_{16}\}Cl_{24}(TbCl_3)_4$			
R−T	2.754−2.857, ⟨d⟩ = 2.809	1.59−2.94	2.12	203.49	35.3
R−R	3.629−4.091, ⟨d⟩ = 3.771	0.01−0.19	0.10	19.42	3.4
R−X	2.573−2.929, ⟨d⟩ = 2.777	0.42−1.76	0.87	332.50	57.2
T−T	3.242−3.243, ⟨d⟩ = 3.243	0.80−0.97	0.86	20.69	3.6
		$\{Ir_4Tb_{16}\}Br_{24}(TbBr_3)_4$			
R−T	2.742−2.858, ⟨d⟩ = 2.806	2.01−2.88	2.41	230.99	37.4
R−R	3.662−4.277, ⟨d⟩ = 3.845	0.01−0.16	0.11	22.58	3.7
R−X	2.714−3.127, ⟨d⟩ = 2.915	0.39−1.67	0.90	345.66	56.0
T−T	3.397−3.404, ⟨d⟩ = 3.400	0.77−0.78	0.77	18.53	3.0
		$\{Rh_4Tb_{16}\}Br_{24}(TbBr_3)_4$			
R−T	2.721−2.836, ⟨d⟩ = 2.785	1.91−2.49	2.17	208.72	34.0
R−R	3.699−4.272, ⟨d⟩ = 3.859	0.01−0.20	0.14	27.82	4.5
R−X	2.731−3.101, ⟨d⟩ = 2.915	0.46−1.78	0.95	365.54	59.6
T−T	3.521−3.524, ⟨d⟩ = 3.522	0.49−0.49	0.49	11.71	1.9

[a]Details of the crystal structures have been reported elsewhere.[23]

Table 4. Distance Ranges, −ICOHP/Bond Ranges, Average −ICOHP/Bond, Cumulative −ICOHP/Cell, and Percentage Contributions for Tetragonal $\{Ir_4Sc_{16}\}Cl_{24}(ScCl_3)_4$, $\{Os_4Sc_{16}\}Cl_{24}(ScCl_3)_4$, $\{Ru_4Sc_{16}\}Cl_{24}(ScCl_3)_4$, and $\{Ru_4Gd_{16}\}Br_{24}(GdBr_3)_4$[a]

	distance [Å]	−ICOHP/bond range [eV/bond]	ave −ICOHP/bond [eV/bond]	cum −ICOHP/per cell	contribution [%]
		$\{Ir_4Sc_{16}\}Cl_{24}(ScCl_3)_4$			
R−T	2.559−2.698, ⟨d⟩ = 2.634	1.65−2.93	2.16	207.43	33.6
R−R	3.343−3.868, ⟨d⟩ = 3.513	0.01−0.14	0.08	15.22	2.7
R−X	2.397−2.849, ⟨d⟩ = 2.602	0.37−1.71	0.95	364.50	59.1
T−T	2.978−2.979, ⟨d⟩ = 2.978	1.18−1.39	1.25	29.93	4.9
		$\{Os_4Sc_{16}\}Cl_{24}(ScCl_3)_4$			
R−T	2.575−2.725, ⟨d⟩ = 2.654	1.64−3.20	2.26	216.65	33.5
R−R	3.298−3.868, ⟨d⟩ = 3.521	0.01−0.20	0.09	17.26	2.7
R−X	2.395−2.868, ⟨d⟩ = 2.601	0.35−1.72	0.98	375.30	58.0
T−T	2.918−2.919, ⟨d⟩ = 2.919	1.49−1.73	1.57	37.61	5.8
		$\{Ru_4Sc_{16}\}Cl_{24}(ScCl_3)_4$			
R−T	2.547−2.706, ⟨d⟩ = 2.632	1.51−2.96	2.08	200.01	31.6
R−R	3.298−3.854, ⟨d⟩ = 3.513	0.01−0.21	0.10	20.74	3.28
R−X	2.397−2.853, ⟨d⟩ = 2.597	0.37−1.73	1.01	386.70	61.1
T−T	2.966, ⟨d⟩ = 2.966	0.99−1.22	1.07	25.59	4.0
		$\{Ru_4Gd_{16}\}Br_{24}(GdBr_3)_4$			
R−T	2.757−2.850, ⟨d⟩ = 2.813	2.11−2.78	2.47	237.01	35.5
R−R	3.655−4.284, ⟨d⟩ = 3.875	0.01−0.26	0.16	31.69	4.8
R−X	2.735−3.142, ⟨d⟩ = 2.923	0.41−1.50	1.00	383.12	57.6
T−T	3.433−3.436, ⟨d⟩ = 3.434	0.6169−0.6346	0.62	14.95	2.2

[a]Details of the crystal structures have been reported elsewhere.[23]

Examining the −COHP curves for the tetragonal structures unveils that the narrow R s and T s bands can be assigned to R−T and T−T bonding interactions, respectively. Additionally, significant R−X bonding interactions are situated between −4.66 and −1.53 eV for $\{Rh_4Tb_{16}\}Br_{24}(TbBr_3)_4$ and between −4.88 and −0.79 eV for $\{Ir_4Tb_{16}\}Br_{24}(TbBr_3)_4$ and range from −4.66 to −0.87 eV for $\{Ru_4Gd_{16}\}Br_{24}(GdBr_3)_4$. Because of the increased electronegativity from Br (7.59) to Cl (8.30),[42] R−X bonding interactions in the chlorides are lower in energy than those in the isostructural bromides [between −5.48 and −1.87 eV for $\{Ir_4Tb_{16}\}Cl_{24}(TbCl_3)_4$, between −5.75 and −1.42 eV for $\{Ir_4Sc_{16}\}Cl_{24}(ScCl_3)_4$, between −5.95 and −1.45 eV for $\{Os_4Sc_{16}\}Cl_{24}(ScCl_3)_4$, and between −5.77 and −1.41 eV for $\{Ru_4Sc_{16}\}Cl_{24}(ScCl_3)_4$]. Moreover, R−X interactions cross from bonding to antibonding states in energy regions from −2.40 to −1.91 eV for the chlorides and from −1.76 to −1.71 eV for all Br-containing compounds [except $\{Ir_4Tb_{16}\}Br_{24}(TbBr_3)_4$]. Note that additional antibonding R−X interactions are located in the energy regions near E_F.

Significant R−T interactions are evident near E_F and the R−X interactions. For instance, sizable Os−Sc interactions are located between −2.13 and −1.44 eV in tetragonal $\{Os_4Sc_{16}\}Cl_{24}(ScCl_3)_4$, while notable Ir−Sc interactions are located between −2.90 and −1.87 eV in the isostructural Ir compounds. Under consideration of Pearson's electronegativities,[42] in which Ir (5.4) is more electronegative than Os (4.9), less electron withdrawal from the endohedral Os atom can be expected and, accordingly, Os−Sc bonding interactions are shifted to higher energy regions rather than in the Ir-containing compound. Note that the states located near the Fermi Level

dx.doi.org/10.1021/ic502374y | Inorg. Chem. 2015, 54, 1026−1037

are occupied completely for group 9 and only partially for group 8 interstitials. R−T interactions contribute 33−38% to the total bonding, whereas the largest percentages to the total bonding capacities of the tetragonal $\{T_4R_{16}\}X_{24}(RX_3)$-type structures originate from R−X interactions (see Tables 3 and 4). Although the occupation of antibonding R−X states at relatively low energies and the comparatively small R−X −ICOHP values indicate less bonding character relative to the R−T interactions, the higher R−X bond frequencies bring about the largest percentage contributions to the total bonding capacities (see Tables 3 and 4). Also, the percentage contributions of the R−R interactions to the total −ICOHP depend strongly on the nature of the rare-earth metal especially the sizes of their orbitals. For instance, R−R interactions in tetragonal $\{Ir_4Tb_{16}\}Cl_{24}(TbCl_3)_4$ show higher percentage contributions to the total −ICOHP (3.4%, 0.10 eV) than those in isostructural $\{Ir_4Sc_{16}\}Cl_{24}(ScCl_3)_4$ (2.5%, 0.08 eV; see Tables 3 and 4).

Here again, significant bonding arises from the heteroatomic R−X and R−T interactions, while the homoatomic R−R and T−T interactions play a subordinate role. Therefore, the overall bonding in the $\{T_4R_{16}\}$ tetramers is better described in Brewer's sense of polar intermetallic bonding rather than in Cotton's definition of metal clusters.[39] Although R−R and T−T interactions contribute 3.6−4.9% and 1.9−3.7%, respectively, to the total −ICOHP, the latter were previously shown to play decisive roles in the distortions of the $\{T_4R_{16}\}$ tetramers.[28] In particular, geometrical restraints and, even more importantly, electronic constrictions were shown to induce distortions of the tetramers, as represented by Figure 10. Because of an increasing

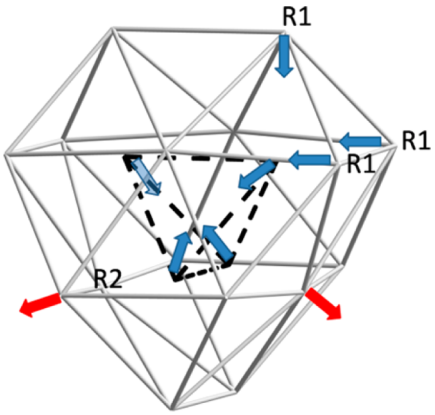

Figure 10. Representation of the "breathing distortion" within a prototypical tetramer in a $\{T_4R_{16}\}X_{24}(RX_3)_4$-type structure. The R1 atoms (Tb1, Tb2, and Tb3 sites; see the text) reside on the vertices, whereas the R2 atoms (Tb4 sites) are located in the centers of the hexagonal faces.

distortion, a t_1 set becomes more R2−T antibonding, while an a_1 orbital is stabilized because of higher T−T bonding and less R1−T antibonding effects.[28] To recognize the trends in the distortions of the $\{T_4R_{16}\}$ tetramers, the magnitude of the *trans*-R1−T−R2 angles was shown to provide conclusive evidence accounting for the strength of the breathing distortion.[28] Because the T−T distances are significantly shorter in $\{Ir_4Tb_{16}\}Br_{24}(TbBr_3)_4$ than in isostructural $\{Rh_4Tb_{16}\}Br_{24}(TbBr_3)_4$ [$\langle d\rangle$(Ir−Ir) = 3.400 Å; $\langle d\rangle$(Rh−Rh) = 3.522 Å] and the sizes of the *trans*-R1−T−R2 angles decrease in the same direction [∠(Tb1−Ir−Tb2) = 163.57°; ∠(Tb1−Rh−Tb2) = 167.17°], we have analyzed the T−T interactions for these structures.

Examining the T−T −ICOHP values for the tetragonal $\{T_4Tb_{16}\}Br_{24}(TbBr_3)_4$ (T = Rh, Ir) structures reveals that the Ir−Ir bonding interactions have larger percentage contributions to the total −ICOHP (Ir−Ir: 3.0%, ICOHP/bond 0.78 eV) rather than the analogous Rh−Rh contacts (Rh−Rh: 1.9%, ICOHP/bond 0.49 eV). This correlates with compression of the crystallographic Tb1, Tb2, and Tb3 sites (R1) toward the centers of the clusters, whereas the Tb4 sites (R2) are elongated from the centers of the octahedra (see Figure 10). Furthermore, this distortion is also clearly recognizable from the interatomic distances (see Table 5). Notably, the strengths

Table 5. Selected Interatomic Distances in Tetragonal $\{T_4Tb_{16}\}Br_{24}(TbBr_3)_4$ (T = Rh, Ir)

ave distance [Å]	T−T	T−Tb1	T−Tb2	T−Tb3	T−Tb4
$\{Rh_4Tb_{16}\}Br_{24}(TbBr_3)_4$	3.522	2.742	2.760	2.775	2.830
$\{Ir_4Tb_{16}\}Br_{24}(TbBr_3)_4$	3.400	2.721	2.742	2.759	2.853

of the distortions also increase from $\{Ir_4Sc_{16}\}Cl_{24}(ScCl_3)_4$ [15 CBEs; ∠(R1−T−R2) = 159.2°] to $\{Ru_4Sc_{16}\}Cl_{24}(ScCl_3)_4$ [14 CBEs; ∠(R1−T−R2) = 158.3°] to $\{Os_4Sc_{16}\}Cl_{24}(ScCl_3)_4$ [14 CBEs; ∠(R1−T−R2) = 156.6°], which may alleviate the predicted electronic instabilities for the two latter systems. Comparatively, tetragonal $\{Ru_4Y_{16}\}X_{20}$ (X = Br, I; 15 CBEs) with their closed-shell configurations show only modest distortions of the tetramers.[28]

IV. CONCLUSIONS

Herein, the electronic structures of prototypical T-centered R cluster halides composed of $\{T_4R_{16}\}$ tetramers have been analyzed utilizing DFT-based methods. Analyses of the overlap interactions derived from the diverse −ICOHP values and their percentages to the total bonding capabilities indicate significant bonding populations between the heteroatomic R−T and R−X contacts, whereas the homoatomic R−R and T−T bonding is a minor, but evident, factor in these structures. Additional examinations of the energy regions near E_F revealed that these states originate primarily from the cluster-based R−T contacts, which are higher in energy relative to the R−X interactions. In the investigations of the states near E_F, gaps associated with closed-shell configurations were identified for CBE counts of 15 electrons. Accordingly, these structures attempt to optimize chemical bonding through an electronically favorable situation, which can be regarded as the origin for the "15-electron-rule". Although these deliberations can be taken into account for a broad number of T-centered R cluster halides with $\{T_4R_{16}\}$ tetramers, there are still deviations from this rule. To understand the origin of these deviations, we analyzed the electronic structures for prototypical examples of such compounds.

In the case of the cubic $\{Ru_4Ho_{16}\}I_{24}(Ho_4I_4)$ structure (16 CBEs), an electron partition scheme of 15 + 1 CBEs appears to be more appropriate to emphasize the overall bonding situation because one electron per f.u. was shown to reside between the R−R and R−X contacts of the empty ($\{\square Ho_4\}I_4$) tetrahedra. For the $\{Ir_4Y_{16}\}Br_{24}(YBr_3)_4$-type structures, E_F falls in a gap, indicating electronic stabilities for 15 CBEs. Removing one CBE from this system intercapsulating group 8 interstitials places E_F at a peak of the DOS, an electronically unfavorable situation, yet these structures may alleviate their expected

dx.doi.org/10.1021/ic502374y | Inorg. Chem. 2015, 54, 1026−1037

electronic instabilities through distortions of the $\{T_4R_{16}\}$-type tetramers.

As of today, $\{T_4R^c{}_{10}R_6^e\}$-type tetramers have been observed solely for the compounds $\{Ru_4Gd_{16}\}Br_{23}$ and $\{B_4Tb_{16}\}Br_{23}$. In the case of monoclinic $\{Ru_4Gd_{16}\}Br_{23}$, E_F is placed at a peak of the DOS, which typically indicates an electronically unfavorable situation, yet this compound has been obtained in reasonable yields.[23] Furthermore, this electronic instability seems to correlate to a single occupation of a cluster-based MO, which is alleviated through structural distortions within the rhomboid-shaped $\{Ru_4Gd_{16}\}$ tetramers.

■ ASSOCIATED CONTENT

Supporting Information

Plots of the projected DOS (Figures S1−S12) as well as −ICOHP/distance comparisons (Tables S13−S24) for all interactions and for cubic $\{Ru_4Ho_{16}\}I_{24}(Ho_4I_4)$, tetragonal $\{Ru_4Y_{16}\}X_{20}$ (X = Br, I), $\{Ir_4Tb_{16}\}Cl_{24}(TbCl_3)_4$, $\{T_4Tb_{16}\}$-$Br_{24}(TbBr_3)_4$ (T = Rh, Ir), $\{T_4Sc_{16}\}Cl_{24}(ScCl_3)_4$ (T = Ru, Os, Ir), and $\{Ru_4Gd_{16}\}Br_{24}(GdBr_3)_4$, as well as orthorhombic $\{Ir_4Y_{16}\}Br_{24}$ and monoclinic $\{Ru_4Gd_{16}\}Br_{23}$. This material is available free of charge via the Internet at http://pubs.acs.org.

■ AUTHOR INFORMATION

Corresponding Author

*E-mail: gerd.meyer@uni-koeln.de or ghmeyer@iastate.edu.

Notes

The authors declare no competing financial interest.

■ ACKNOWLEDGMENTS

This work was generously supported by the Deutsche Forschungsgemeinschaft, Bonn, Germany (SFB 608, Complex Transition Metal Compounds with Spin and Charge Degrees of Freedom and Disorder) as well as by the University of Cologne through direct funds to the Chair. S.S. is grateful for a Chemiefonds-Doktorandenstipendium by Fonds der Chemischen Industrie eV, Frankfurt aM, Germany, while T.B. is thankful for a Ph.D. stipend from Studienstiftung des Deutschen Volkes eV.

■ DEDICATION

Dedicated to the memory of Professor John D. Corbett, Pioneer of this Chemistry.

■ REFERENCES

(1) Corbett, J. D. *Inorg. Chem.* **2010**, *49*, 13−28.
(2) (a) Wade, K. *J. Chem. Soc. D* **1971**, *15*, 792−793. (b) Wade, K. *Inorg. Nucl. Chem. Lett.* **1972**, *8*, 559−562.
(3) (a) Zintl, E. *Angew. Chem.* **1939**, *52*, 1−6. (b) Klemm, W.; Busmann, E. *Z. Anorg. Allg. Chem.* **1963**, *319*, 297−311.
(4) (a) Corbett, J. D. *Angew. Chem., Int. Ed.* **2000**, *39*, 670−690. (b) Corbett, J. D. *Inorg. Chem.* **2000**, *39*, 5178−5191.
(5) (a) Whangbo, M.-H.; Lee, C.; Köhler, J. *Angew. Chem., Int. Ed.* **2006**, *45*, 7465−7469. (b) Köhler, J.; Whangbo, M.-H. *Solid State Sci.* **2008**, *10*, 444−449. (c) Miller, G. J.; Schmidt, M. W.; Wang, F.; You, T. S. Quantitative Advances in the Zintl-Klemm Formalism. In *Zintl Phases: Principles and recent developments*; Fässler, T. F., Ed.; Springer: Berlin, 2011; Vol. *139*, pp 1−55.
(6) Huang, B.; Corbett, J. D. *Solid State Sci.* **1999**, *1*, 555−565.
(7) Lin, Q.; Mishra, T.; Corbett, J. D. *J. Am. Chem. Soc.* **2013**, *135*, 11023−11031.
(8) Meyer, G. *Z. Anorg. Allg. Chem.* **2008**, *634*, 2729−2736.
(9) Corbett, J. D. *J. Alloys Compd.* **2006**, *418*, 1−20.
(10) Corbett, J. D. *J. Alloys Compd.* **1995**, *229*, 10−23.
(11) Meyer, G. Rare Earth Metal Cluster Complexes. In *The Rare Earth Elements*; Atwood, D. A., Ed.; John Wiley & Sons: New York, 2012.
(12) Simon, A.; Mattausch, Hj.; Ryazanov, M.; Kremer, R. K. *Z. Anorg. Allg. Chem.* **2006**, *632*, 919−929.
(13) Meyer, G. *Chem. Rev.* **1988**, *88*, 93−107.
(14) Simon, A.; Mattausch, H. Low-Valence Compounds of the Lanthanoids. In *Comprehensive Inorganic Chemistry II*; Reedijk, J., Poeppelmeier, K., Eds.; Elsevier: New York, 2013; pp 535−581.
(15) Rustige, C.; Brühmann, M.; Steinberg, S.; Meyer, E.; Daub, K.; Zimmermann, S.; Wolberg, M.; Mudring, A.-V.; Meyer, M. *Z. Anorg. Allg. Chem.* **2012**, *638*, 1922−1931.
(16) Steinberg, S.; Brgoch, J.; Miller, G.; Meyer, G. *Inorg. Chem.* **2012**, *51*, 11356−11364.
(17) Steinberg, S.; Valldor, M.; Meyer, G. *J. Solid State Chem.* **2013**, *206*, 176−181.
(18) Zimmermann, S.; Brühmann, M.; Casper, F.; Heyer, O.; Lorenz, T.; Felser, C.; Mudring, A.-V.; Meyer, G. *Eur. J. Inorg. Chem.* **2010**, 2613−2619.
(19) (a) Dorhout, P. K.; Corbett, J. D. *J. Am. Chem. Soc.* **1992**, *114*, 1697−1701. (b) Ahn, K.; Hughbanks, T.; Rathnayaka, K. D. D.; Naugle, D. G. *Chem. Mater.* **1994**, *6*, 418−423.
(20) Ebihara, M.; Martin, J. D.; Corbett, J. D. *Inorg. Chem.* **1994**, *33*, 2079−2084.
(21) Payne, M. W.; Ebihara, M.; Corbett, J. D. *Angew. Chem., Int. Ed. Engl.* **1991**, *30*, 856−858.
(22) Steinwand, S. J.; Corbett, J. D. *Inorg. Chem.* **1996**, *35*, 7056−7067.
(23) Steinberg, S.; Zimmermann, S.; Brühmann, M.; Meyer, E.; Rustige, C.; Wolberg, M.; Daub, K.; Bell, T.; Meyer, G. *J. Solid State Chem.* **2014**, *219*, 159−167.
(24) Mattausch, Hj.; Vajenine, G. V.; Oeckler, O.; Kremer, R. K.; Simon, A. *Z. Anorg. Allg. Chem.* **2001**, *627*, 2542−2546.
(25) Hughbanks, T. *Prog. Solid State Chem.* **1989**, *19*, 329−372.
(26) Hughbanks, T.; Rosenthal, G.; Corbett, J. D. *J. Am. Chem. Soc.* **1986**, *108*, 8289−8290.
(27) Sweet, L. E.; Roy, L. E.; Meng, F.; Hughbanks, T. *J. Am. Chem. Soc.* **2006**, *128*, 10193−10201.
(28) Steinwand, S. J.; Corbett, J. D.; Martin, J. D. *Inorg. Chem.* **1997**, *36*, 6413−6422.
(29) Gupta, S.; Meyer, G.; Corbett, J. D. *Inorg. Chem.* **2010**, *49*, 9949−9957.
(30) Andersen, O. K. *Phys. Rev. B* **1975**, *12*, 3060−3083.
(31) Andersen, O. K.; Jepsen, O. *Phys. Rev. Lett.* **1984**, *53*, 2571−2574.
(32) Krier, G.; Jepsen, O.; Burkhardt, A.; Andersen, O. K. *TB-LMTO-ASA Program*, 4.7th ed.; Max-Planck-Institut für Festkörperforschung: Stuttgart, Germany, 1995.
(33) von Barth, U.; Hedin, L. *J. Phys. C: Solid State Phys.* **1972**, *5*, 1629−1642.
(34) Lambrecht, W. R. L.; Andersen, O. K. *Phys. Rev. B* **1986**, *34*, 2439.
(35) Dronskowski, R.; Blöchl, P. E. *J. Phys. Chem.* **1993**, *97*, 8617−8624.
(36) Börnsen, N.; Meyer, B.; Grotheer, O.; Fähnle, M. *J. Phys.: Condens. Matter* **1999**, *11*, L 287.
(37) Dronskowski, R. *Computational Chemistry of Solid State Materials*; Wiley-VCH: Weinheim, Germany, 2005.
(38) Brewer, L.; Wengert, P. R. *Metall. Trans.* **1973**, *4*, 83−104.
(39) (a) Cotton, F. A. *Acc. Chem. Res.* **1969**, *2*, 240−247. (b) Cotton, F. A. *J. Chem. Educ.* **1983**, *60*, 713−720.
(40) Warkentin, E.; Bärnighausen, H. *Z. Anorg. Allg. Chem.* **1979**, *459*, 187−200.
(41) (a) Palasyuk, A.; Meyer, G. *Z. Anorg. Allg. Chem.* **2004**, *630*, 1691. (b) Gerlitzki, N.; Meyer, G.; Mudring, A.-V.; Corbett, J. D. *J. Alloys Compd.* **2004**, *380*, 211−218. (c) Meyer, G.; Palasyuk, A. *Inorg. Chem. in Focus* **2006**, *3*, 45−60.
(42) Pearson, R. G. *Inorg. Chem.* **1988**, *27*, 734−740.